LRP 587/97 Octobre 1997

ELECTRON BEAM INSTABILITIES IN GYROTRON BEAM TUNNELS

M. Pedrozzi, S. Alberti, J. P. Hogge, M.Q. Tran,
and T.M. Tran

Submitted for publication in
Physics of Plasmas

Electron beam instabilities in gyrotron beam tunnels

M. Pedrozzi, S. Alberti, J.P. Hogge, M.Q. Tran, and T.M. Tran

Centre de Recherches en Physique des Plasmas,

Association EURATOM - Confédération Suisse,

Ecole Polytechnique Fédérale de Lausanne,

CRPP-PPB CH-1015 Lausanne

ABSTRACT

Electron beam instabilities occuring in a gyrotron electron beam can induce an energy spread which might significantly deteriorate the gyrotron efficiency. Three types of instabilities are considered to explain the important discrepancy found between the theoretical and experimental efficiency in the case of quasi-optical gyrotrons (QOG): the electron cyclotron maser instability, the Bernstein instability and the Langmuir instability. The low magnetic field gradient in drift tubes of QOG makes that the electron cyclotron maser instability can develop in the drift tube at very low electron beam currents. Experimental measurements show that with a proper choice of absorbing structures in the beam tunnel, this instability can be suppressed. At high beam currents, the electrostatic Bernstein instability can induce a significant energy spread at the entrance of the interaction region. The induced energy spread scales approximately linearly with the electron beam density and for QOG one observes that the beam density is significantly higher than the beam density of an equivalent cylindrical cavity gyrotron.

I. INTRODUCTION

In high power microwave sources such as the gyrotron and the free electron laser, the conversion efficiency from free kinetic energy of a magnetized electron beam to electromagnetic energy is strongly dependent on the electron beam quality at the entrance of the interaction region. In general, the electron beam quality can be characterized by the relative spreads of two independent variables, $\beta_{\|} = v_{\|}/c$, the normalized parallel velocity (c is the speed of light) and the energy γ where $\gamma = 1/\sqrt{1-\beta_{\|}^2-\beta_{\perp}^2}$, with $\beta_{\perp} = v_{\perp}/c$ being the normalized perpendicular velocity. The relative spreads are defined as $\delta\beta_{\|} = \Delta\beta_{\|}/\langle\beta_{\|}\rangle$ and $\delta\gamma = \Delta\gamma/\langle\gamma\rangle$ with $\Delta...$ and $\langle...\rangle$ being the rms standard deviation and mean value respectively. Two classes of beam quality are commonly distinguished, $\delta\gamma = 0$ (monoenergetic beam) and $\delta\gamma \neq 0$.

If no instabilities occur between the cathode and the interaction region, the electron beam can be considered as almost monoenergetic since the energy spread induced by the DC space charge accross the thin beam is negligible. In this case the parallel velocity spread can be directly converted into pitch angle spread $\delta\alpha$, with $\alpha = \beta_{\perp}/\beta_{\|}$. The origin of pitch angle spread is mainly due to beam optics effects such as cathode surface roughness [1,2] and laminar beam flow after the cathode which breaks the adiabatic constancy of the magnetic moment [3]. Beam diagnostics have been employed recently to measure the beam velocity distribution in gyrotrons. They are based on the retarding potential technique [4,5] and the electron cyclotron emission [6]. Both methods provide only the parallel velocity spread and assume a mono-energetic beam in order to estimate the pitch angle spread.

On the other hand, energy spread can be generated only if an instability develops between the gun and the interaction region and in this paper, three different types are considered. First, the electron cyclotron maser instability (ECMI) itself, on which the generation of rf power in the gyrotron relies. This instability is of electromagnetic na-

ture and for a gyrotron operating close to cutoff, in the resonator region it converts the rotational kinetic energy of the electron beam into elctromagnetic energy. Outside the well defined resonator region, the ECMI could also become unstable in one or more of the different beam transport structures between the electron gun and the collector. Its signature is the presence of parasitic radio frequency radiation with a frequency close to the electron cyclotron frequency. By parasitic one means rf oscillations with frequencies not related to the well defined modes supported by a Fabry-Pérot resonator, for a quasi-optical gyrotron (QOG), or the cavity in a cylindrical cavity grotron (CCG). Such oscillations have been observed in the QOG [7–9] as well as in a cylindrical cavity configuration [10]. It will be shown in this paper that the excitation of these oscillations is strongly influenced by the beam tunnel structure. The second instability is the electrostatic Bernstein instability BI [11–14] which, on the contrary of the previous one, can develop independently of an external electromagnetic structure like the beam tunnel. It is therefore an intrinsic property of the electron beam and consequently more difficult to suppress. The third instability is the Langmuir instability [15] which is also of electrostatic nature, but needs a slow wave structure to get unstable. Such a structure is present in gyrotron beam tunnels formed by a periodic stack of conducting and dielectric rings (absorbing material) which is commonly used for suppressing the electromagnetic instability [16]. Table I lists the dependency on the main experimental parameters of the linear temporal growth rates ω_i and frequencies $\omega_r/2\pi$ for the three instabilities. For the typical electron beam parameters used in the design and operation of gyrotrons, the growth rates of the three instabilities are listed in increasing order in Table I, with the ECM instability being the most unstable.

The global effect of these instabilities on the electron beam properties is summarized in Fig. 1, where, on the basis of single-mode calculations with a Gaussian rf profile and for a pencil beam, the effect of a total energy spread on the interaction efficiency is shown. The relevant quantity is the efficiency reduction $\eta(\delta\gamma, \beta_\parallel)/\eta_0$, where

$\eta_0 = \eta(\delta\gamma = 0, \delta\beta_{\|} = 0)$ is the electronic efficiency for a monoenergetic beam. One observes in this figure that the gyrotron efficiency is strongly affected by the energy spread $\delta\gamma$ whereas the dependency on parallel velocity spread $\delta\beta_{\|}$ is weak. This is due to the fact that the gyrotron interaction is strongly dependent on the detuning parameter, $\Delta_g = 1 - \frac{\Omega_{ce}}{\gamma 2\pi f_g}$ which is itself dependent on γ ($\Omega_{ce} = eB_0/m_0$ is the non-relativistic cyclotron frequency with e and m_0 being the electron charge and rest mass respectively, B_0 is the dc magnetic field and f_g is the gyrotron rf frequency). Experimental studies of QOG show a systematic discrepancy between the experimental and theoretical efficiency [7,8,18], whereas in cylindrical cavity gyrotrons, a good agreement between theory and experiment is found (Table II). In QOG gyrotrons, the observation of parasitic oscillations in the beam tunnel suggests an important electron beam degradation which can partially explain the discrepancy between the calculated and measured efficiencies. Since the data of Fig. 1 were computed with a Gaussian rf profile, its relevancy also encompasses cylindrical cavity gyrotrons with a high quality factor cavity.

In section II of this paper, the experimental setup is presented. Section III is devoted to the experimental results for the ECM instability observed in a QOG beam tunnel. A discussion of the effect on the electron beam of the different instabilities is made in section IV. Section V will finally conclude the paper.

II. EXPERIMENTAL SETUP

In this section the experimental setup will be outlined. In part A) the general experimental setup with the diagnostics for the measurement of the parasitic oscillations excited in the beam tunnel will be described and in part B) details of the different beam tunnels configurations will be given.

A. Global setup

A schematic of the QOG is given in Fig. 2, and a detailed description of the gun and magnetic field configuration can be found in Ref. [7]. The laminar electron beam is produced by a triode magnetron injection gun (MIG). The electrons emitted from a temperature limited cathode are accelerated by a DC voltage ($V_b \simeq 70$kV), adiabatically compressed by the applied magnetic dc-field (compression $\simeq 20$) and guided through a beam tunnel to reach the interaction region where the Fabry-Pérot resonator is placed. The electron beam has an annular cross section with a mean radius $r_b = 2.4$mm in the interaction region. The resonator axis is perpendicular to the beam propagation, so that in the interaction region, the first metallic boundary felt by the electron beam in the radial direction is the vacuum vessel (radius = 185mm). For such a configuration, it has been shown in ref. [21] that the beam depression in the interaction region is mainly determined by the spacing between the beam ducts. The oscillation on a resonator mode could be prevented by inserting a plate of absorbing material (Macor) in front of the mirrors. The magnetic field profile, as well as a more detailed description of the experimental layout is shown in Fig. 3. On this figure, the dc magnetic field gradient in the beam tunnel region is also shown. Due to the large size of the magnet system required to accomodate the Fabry-Pérot resonator, the magnetic field gradients in QOG's are low compared to those of cylindrical cavity gyrotrons. Consequently, for QOG, the electron beam travels in a beam tunnel for longer distances than in an equivalent cylindrical cavity configuration. After the free space propagation section, the electron beam travels again in a beam tunnel of variable cross section until it reaches the collector. In order to prevent parasitic oscillations to occur in the beam tunnel after the free propagation section, for some experiments the portion of beam tunnel labeled "section 3" in Fig. 3 was removed.

Different diagnostics have been used for the measurement of the parasitic oscillations

excited inside the beam tunnel. For mode identification, frequency measurements with a resolution of 100kHz were performed with a series HP70000 spectrum analyzer. The WR10 horn used for the detection of the rf signal was located on one of the viewing ports shown in Fig. 2. For an estimation of the rf power emitted by the parasitic oscillations, a Scientech laser calorimeter was modified by adding a thicker absorptive layer (3M Nextel spray) to maximize the absorption in the 100 GHz range. This calorimeter was located behind the collector window (Pos. 11 on Fig. 2) and its position with respect to the beam tunnel, where the parasitic rf power is generated, allowed only a relative power measurement. Measurements of the parallel velocity distribution function of the electron beam, based on electron cyclotron emission, have been performed and the diagnostic is described in Ref. [6].

B. Beam tunnels

Three different types of beam tunnels (sections 1 and 2 in Fig. 3) have been studied.

The simplest configuration consists of a section ($L = 220$mm) of constant radius ($r_w = 5$mm) OFHC copper tube. It has been choosen since it allows a relatively simple modeling of the interaction between the electron beam and the electromagnetic modes (EM) supported by the beam tunnel. These modes are the $TE_{m,n}$ and $TM_{m,n}$ modes of a cylindrical waveguide (m and n are the azimuthal and radial index respectively), with the most unstable modes for the ECM instabilty being the $TE_{m,n}$ modes near cutoff. The longitudinal EM field profile can be assumed to be that of a standing wave, since at both ends of this section there are important discontinuities causing significant reflections. Using a scattering matrix code (CASCADE [22]) the resonant frequency and diffractive quality factor of the $TE_{m,n,q}$ mode (q is the longitudinal index) have been calculated for the real geometry and are shown in Fig. 4 for the mode $TE_{0,3,q}$ which has been observed experimentally. The resonant frequencies correspond to the resonances

of a closed cylindrical cavity and are given by $f_{m,n,q} = \omega_r/2\pi = \frac{1}{2\pi}c\sqrt{(\chi_{m,n}/r_w)^2 + k_z^2}$ with $\chi_{m,n}$ being the n^{th} zero of $J'_m(x)$ and $k_z = q\pi/L$ is the longitudinal wave number. A good approximation of the diffractive quality factor is $Q_{diff} \simeq \frac{\omega_r L}{v_g(1-|R_1R_2|)}$ where $v_g = \frac{\pi q c^2}{\omega_r L}$ is the group velocity and R_1 and R_2 are the reflection coefficients at both ends of the beam tunnel section. For resonant frequencies close to cutoff, the ohmic quality factor can be approximated by $Q_\Omega \simeq \frac{\omega_r^3}{c^3}\frac{Z_0 r_w^3}{2\chi_{mn}^2 R_s}(1-(m/\chi_{mn})^2)$, where $Z_0 = 377\Omega$ is the vacuum impedance and R_s is the surface resistivity. Within this approximation, Q_Ω is independent of the longitudinal index q. The total quality factor, which is relevant for the calculation of the starting current, is given by: $1/Q_{tot} = 1/Q_{diff} + 1/Q_\Omega$. Notice that for this beam tunnel configuration, the total quality factor is comparable to the total quality factor of the Fabry-Pérot resonator ($Q_{tFP} \simeq 10000$) [7].

The two other configurations of beam tunnels are shown in Fig. 5 and are both dielectrically loaded. Both structures consist of a stack of copper and dielectric rings. The inner diameter of the copper ring, r_{ci} is smaller than the inner diameter of the dielectric ring r_{di} in order to avoid charge build up inside the dielectric caused by an eventual electron beam interception. For both structures the smallest inner radius of the metallic rings is equal to the radius of the smooth beam duct ($r_w = 5$mm) and in some cases the inner diameter of the copper rings were wedge shaped as shown in Fig. 5 b) (section1). The dielectric properties of the different materials used are listed in Table III. The calculation of the resonant modes and the losses can be made with CASCADE, with the only restriction that the axes of symmetriy of each element have to be aligned (no off-axis element). For symmetric TM modes ($m = 0$) with the additional restriction that $r_{ci} = r_{di}$ a model has been developed by Tigelis et al. [16]. For the case of the periodic beam tunnel (Fig. 5a)), the axial dependence of the azimuthal component of the electric field, E_θ, calculated with CASCADE, is shown for a resonant TE mode in Fig. 6. The resonant frequency of this mode is 97.9GHz and in the calculation, it has

been assumed that $r_{ci} = r_{di}$. For $r < r_{ci}$, its transverse structure is similar to the TE_{03} profile of a smooth beam duct with $r_w = r_{ci}$. The short wavelength modulation on the axial profile is due to the presence of the dielectric and one observes that the amplitude of the electric field is larger in the metallic rings. In general, for the periodic structure, the transverse profile of the resonant mode in the vacuum region ($TE^{eq}_{m,n}$ for $r < r_{ci}$) is like the transverse profile of the corresponding mode ($TE_{m,n}$) for the smooth beam duct with $r_{ci} = r_w$. The additional loading caused by the dielectric, is illustrated in Fig. 7, where the total quality factor Q_{tot} ($1/Q_{tot} = 1/Q_{diff} + 1/Q_{\Omega} + 1/Q_{dielectric}$) is plotted against ε_i for MgO-SiC.

The slow-wave property of the periodic structure is shown in Fig. 8 where the dispersion relation of a low frequency fundamental TM mode is shown. The dielectric constant has been taken to be real with $\varepsilon = \varepsilon_r = 7$ and, as shown by Tigelis et al. [16], the imaginary part of ε has only a weak effect on the dispersion relation. The beam line given by $k_z v_z$ is also shown and the intersection with the dispersion relation gives the frequency of an eventual Langmuir instability as it will be discussed later.

The fact that in the periodic beam tunnel, the transverse profile of the resonant modes is weakly affected by the dielectric, has suggested the design of the aperiodic structure(Fig. 5 b)) in order to locally break the coupling between the EM wave and the electron beam. No numerical modeling of the aperiodic structure has been made due to the required CPU time and the difficulty to numerically find the resonant mode of such a structure.

III. EXPERIMENTAL RESULTS

In part A of this section, observations of parasitic oscillations with the Fabry-Pérot resonator in place will be presented. In this configuration, simultaneous excitation of parasitic modes and resonator modes is observed. In part B, experimental results on parasitic oscillations without the Fabry-Pérot resonator will be given for the various

beam tunnel configurations (smooth, dielectrically loaded periodic and aperiodic) as well as measurements of the parallel distribution function for different electron beam regimes.

A. Parasitic Oscillations with Fabry-Pérot resonator

The observation of parasitic oscillations has been made in several QOG experiments with pulse length $t_{rf} \simeq 10$ms [7,8]. For a 100GHz QOG [7], Fig. 9 shows the emitted frequency spectrum and rf-power versus beam current. As indicated, the experimentally measured starting current I_{stFP} for the excitation of $TEM_{0,0,q}$ gaussian modes of the Fabry-Pérot resonator is $I_{stFP} \simeq 1.3$A, at this current the first resonator mode to be excited is the $TEM_{0,0,225}$ oscillating at a frequency of 100.6GHz. For beam currents below I_{stFP}, parasitic emission is observed in the frequency range $97 - 98$GHz. It has been verified that these signals are not associated to resonator modes since they are independent of the mirror separation. For currents higher than I_{stFP} there is coexistence of parasitic and resonator modes. Experimental evidence shows that the emitted rf power in the parasitic mode is strongly decreased by the presence of a resonator mode. A similar result was obtained for the QOG described in Ref. [8].

B. Parasitic Oscillations without Fabry-Pérot resonator

In order to prevent the oscillation on TEM modes defined by the Fabry-Pérot resonator the Macor absorbing plate has been placed in front of one of the two mirrors.

1. Smooth beam tunnel

For the smooth beam tunnel configuration, Fig. 10 shows the emitted spectrum of parasitic oscillations versus magnetic field variation. The $\Delta B_0 = 0\%$ value corresponds

to $B_0 = 4$T and corresponds to the maximum of the axial magnetic field profile ($z = 0.4$m in Fig. 3). In this figure, one observes that the relativistic cyclotron frequency Ω_{ce}/γ ($\gamma = 1.129$), represented by the oblique line, is in general higher than the measured parasitic emission frequency which remains constant (horizontal lines). The pitch angle variation versus ΔB_0 is negligible [$\alpha(\Delta B_0 = -7\%) = 1.08, \alpha(\Delta B_0 = +4\%) = 0.92$] and the electron beam average radius can be taken as constant with $r_b = 2.4$mm ($r_b/r_w = 0.48$). One observes that the emitted frequencies correspond to the TE_{mn} waveguide modes defined by the smooth beam duct which also have a good geometrical coupling with the electron beam. The excitation of these modes is particularly insensitive to magnetic field variations. For a given excited $TE_{m,n}$ mode ($TE_{2,3}$ for example), a finer structure is observed and corresponds to the excitation of different longitudinal modes ($TE_{2,3,q}$). At $\alpha = 0.8$, the smallest beam current at which these oscillations have been observed is $I_{stmin} = 80$mA.

2. Dielectrically loaded beam tunnels

Two types of periodic beam tunnels have been studied, the first one corresponds to Fig. 5a) and has a constant inner radius of 5mm along the entire beam tunnel, whereas the second has a conical output taper as shown in Fig. 3. In both cases, the mode excitation and insensitivity against magnetic field variations is similar to the case of a smooth beam tunnel.

The main effect of the dielectrically loaded beam tunnel on the parasitic mode excitation is observed with the aperiodic structure as it is shown in Fig. 11. With respect to the two previous structures, there is no evident excitation of equivalent TE_{mn} modes of a smooth beam tunnel and in addition, the excited frequency are very sensitive to magnetic field variations. The observed frequency bands separated by $\Delta f = 810 \pm 20$MHz can be explained by the excitation of modes inside the entire vacuum vessel which is possible since the electron beam is not surrounded by a beam tunnel in the interaction

region. With a vacuum vessel diameter of $d \simeq 370$mm one expects a mode separation of $\Delta f = c/2d \simeq 405$MHz, which is approximately half of the measured frequency gap. The important result is that the loaded aperiodic structure suppresses the ECM instability inside the beam tunnel. Figure 12, shows the experimentally measured minimum starting current versus pitch angle $\langle\alpha\rangle$ for all the studied beam tunnel configurations. As pointed out above, for the aperiodic loaded structure, the excitation of parasitic modes does not correspond to mode supported by the beam tunnel. The two sets curves labeled a) and b) correspond to a same beam tunnel structure, but have been taken for two different experimental situations. The set labeled a) corresponds to a situation where the electron beam could be established reliably without problems, whereas the set labeled b) has been measured after a situation were many arcing events where observed.

The correlation between the two sets of starting current curves and the parallel velocity distribution function can be seen in Fig. 13, where the measurements have been performed using the ECE diagnostic. The filled dots, with a measured spread of $\delta\beta_{\|} = 2.7\%$ correspond to the lower starting current curves [set a)] of Fig. 12, correspondingly the open dots, with $\delta\beta_{\|} = 5.7\%$ yield a larger starting current (set a) of Fig. 12). The high sensitivity of the minimum starting current of the ECM instability on $\delta\beta_{\|}$ ($\delta\gamma = 0$) can be associated to excitation of higher order longitudinal modes ($q > 1$) as it has been shown by Kreischer et al. [23]. For both cases, the parasitic oscillations in the beam tunnel were excited and the beam parameters were: $V_b = 62$kV, $\alpha = 1$ and $I_b \simeq 500$mA. Since the ECM instability does not affect the parallel momentum for resonant modes close to cutoff, it is very likely that the parallel velocity spreads are generated in the gun region. In this same figure, the distribution function predicted by a trajectory code is shown. As it is currently observed in gyrotrons [4–6], the measured parallel velocity spreads are significantly larger than the calculated one's.

IV. DISCUSSION

A. ECM instability

For the smooth beam tunnel structure, a linear theory including the axial variation of the magnetic field [24] can be used for calculating the starting current of the parasitic TE_{mn} modes. The starting current is defined as

$$I_{st} = \frac{\omega_r W}{\eta_{lin} V_b Q_{tot}}, \tag{1}$$

with W, V_b and η_{lin} being the rf stored energy in the cavity, the acceleration voltage and linear efficency, respectively. As discussed in reference [24], η_{lin} mainly depends on the geometrical coupling factor between the electron beam and the EM modes, the interaction length and the frequency mismatch (or detuning) between the relativistic electron cyclotron frequency and the rf-frequency.

For our experimental configuration, the annular electron beam radius and $\langle\alpha\rangle$ can be taken as constant in the considered interaction region ($L = 220$ mm). The longitudinal profile of the EM mode on which the interaction takes place, is assumed to be that of a standing wave with an axial dependence of the form $\sin(q\frac{\pi}{L}z)$, where q indicates the longitudinal mode number. Using the actual magnetic field profile, Fig. 14 shows, for the $TE_{2,3}$ mode, the minimum starting current and frequency versus magnetic field variation B/B_0 for the 20 first longitudinal modes. As shown in Fig. 15, the extremely low starting current values of Fig. 14 are mainly due to the strong L^3 dependence of the linear efficiency η_{lin} on the interaction length L. In this figure, the continuous lines are calculated starting currents assuming a constant magnetic field and the $TE_{2,3,1}$ resonant mode. The dotted line represents the starting current calculated by considering an interaction region of $L = 220$mm, but with the axial magnetic field profile of Fig. 3. The significant difference between the calculated and measured starting currents can be associated to the fact that in the calculation one assumes a cold beam ($\delta\alpha = \delta\gamma = 0$),

and that the coupling factor between the rf EM mode excited in the beam tunnel and the detection horn is very weak and makes the measurement of the starting current difficult.

The effect of the axial variation of the magnetic field is similar to the constant magnetic field case but with a shorter equivalent interaction length $L^{eq} < L$. The spectrum of parasitic modes excited in a smooth beam tunnel, is well modeled by the linear theory as it is shown in Fig. 16. In this figure, in part a), the experimentally observed parasitic modes versus pitch angle α are shown and in part b), the minimum starting currents versus α has been calculated for different TE_{mn} modes. Notice that the measurement have been taken with a beam current I_b=1A, which is significantly larger than the minimum starting current shown in Fig. 16b. This might explain the multimode excitation of TE_{42} and TE_{03} observed for $\alpha > 0.7$. Within linear theory, the energy spread scales linearly with the electric field amplitude associated to the rf parasitic oscillation and for the parameters of the present beam tunnel is in the range of $\delta\gamma = 0.4 - 0.6\%$ and corresponds to an interaction efficiency below 5%. As shown in Fig. 1, this values of energy spread can already reduce the interaction efficiency on $TEM_{0,0,q}$ mode supported by the Fabry-Pérot resonator.

As pointed out earlier, the resonant mode transverse structure of the dielectrically loaded periodic beam tunnel, is weakly affected by the dielectric rings. Therefore, compared to the previous analysis, only the total quality factor will be decreased by the presence of the loading. For the longitudinal structure of a resonant mode (TE_{03}^{eq}) shown in Fig. 6, the minimum starting current versus loss factor ε_i is shown in Fig. 7. In order to take into account the actual profile of the resonant mode, the starting current has been calculated using a model developed by Latham et al. [25]. One observes a saturating effect of the total quality factor with respect to the loss factor ε_i. Similarly to the case of the smooth beam tunnel, the minimum starting current is strongly dependent on the interaction length. A quantitative comparison of the calculated minimum starting current with the experimental measurement is difficult due to the observation

that parasitic modes could be excited in the vacuum vessel. Nevertheless the important results are that according to the calculations, the loading with dielectrics on a periodic structure is able to increase the minimum starting current for the excitation of parasitic modes, but for typical beam currents of high power gyrotrons ($I_b > 20$A) the parasitic modes would still be excited in the beam tunnel for the QOG configuration studied here. Experimental evidence shows that the aperiodic structure suppresses the parasitic modes in the beam tunnel. In order to prevent parasitic oscillations in structures other than the beam tunnel, the loading of the vacuum vessel with an absorbing layer (e.g. Titanium dioxide (TiO_2) [26]) is required.

B. Bernstein instability

Due to its electrostatic nature, the Bernstein instability develops itself within the electron beam and does not depend on external boundary conditions like those defined by a beam tunnel. This property makes that, experimentally, the observation of this instability is only made in a very indirect way by measuring the induced energy spread with the ECE diagnostic (see discussion in Ref. [6]), provided that no other instability are excited.

It is shown in ref. [11], that the saturation level of this convective instability has a weak dependence on the magnetic field gradient but a very strong dependence on the electron density which makes this last quantity, the relevant parameter for evaluating the induced energy spread. Figure 17 [11] shows a 2D calculation of the saturated energy spread $\delta\gamma$ versus normalized electron beam density $\omega_{pe}^2/\Omega_{ce}^2$, where $\omega_{pe}/2\pi$ and $\Omega_{ce}/2\pi$ are the electron plasma and cyclotron frequencies, respectively. The external magnetic field is constant. For the beam current levels at which we have observed the parasitic modes associated to an ECM instability, the energy spread induced by the BI is negligible, but assuming that the ECM instabilty has been stabilized by using a aperiodic dielectric loading in the beam tunnel, for high-power gyrotrons, the energy spread induced by

the BI can be significant if the normalized beam density $\omega_{pe}^2/\Omega_{ce}^2$ is larger than 2.10^{-4} (see Fig. 17) at the gyrotron operating current. For a given beam current I_b, the larger beam density found in QOG configurations compared to a cylindrical cavity gyrotron is essentially due to the choice of an average beam radius which is optimized for maximum coupling with the $TEM_{0,0,q}$ mode supported by the Fabry-Pérot resonator. In QOG, the beam radius r_g in the interaction region is choosen such to maximize the geometrical coupling factor $G^{\pm}(r_g) = \frac{1}{2}(1 \pm J_0(2kr_g))$, where J_0 is the 0^{th} order ordinary Bessel function and k is the free space wave vector. In practice, the second or third maxima of $G^{\pm}$ is considered, which yields a normalized density $\omega_{pe}^2/\Omega_{ce}^2$ at $I_b = 10$A of $3. - 5.\ 10^{-4}$. At this current level of 10A, the corresponding normalized density in a cylindrical cavity gyrotron is $0.75\ 10^{-4}$, which is significantly lower than the QOG. 2D calculations of the energy spread induced by the BI and where the actual magnetic field profile is taken into account gives, for $I_b = 20$A, $\delta\gamma$ =0.6% for the QOG [7] and $\delta\gamma$ =0.12% for the CCG [20]. The electron beam density in QOG can be decreased by either increasing the beam radius or making the beam thicker. Optimizations studies of the rf-efficiency for such beams are presently underway.

Numerical simulations performed by Jost et al. [27], for the case of a smooth beam tunnel configuration, shows that when the BI and the ECM instabilities are simultaneously excited, the induced energy spread associated to the BI is always negligible compared to the one induced by the ECM instability.

C. Langmuir instability

The periodic loaded beam tunnel 5a) supports the propagation of a low-frequency (3-5GHz) slow-wave as shown in Fig. 8. The interaction of TM modes with the electron beam is essentially described by the parallel equation of motion $dp_z/dt = -eE_z(z,t)$ where $E_z(z,t)$ is the parallel component of the electric field associated to the TM mode. Within a linear theory [15] the starting current of the instability versus beam tunnel

length is shown in Fig. 18 for a dielectric corresponding to MgO-SiC and for different magnetic field gradients. As for the ECM instability, one observes that the minimum starting current is strongly sensitive to the interaction length, but shows a weak dependence on the magnetic field gradient. In our present configuration, the location of the beam tunnel is such that a gradient of 50 G/mm is a good approximation of the actual magnetic field profile which implies a minimum starting current for this instability of 8-9A if $L_{tot} = 220$mm is considered. No experimental evidence of the excitation of such an instability has been found. The main reason is the fact that the dielectric losses are so important that almost all the generated rf power is dissipated into the dielectric. An estimated value of the ratio between generated and diffracted power is of the order of 10^{-5}. This very small value together with a very weak coupling between any rf-fields generated in the beam tunnel and the detection horn makes that the rf signal is below the detection limit of the diagnostic. The minimum starting current of this instability can be increased by using an aperiodic loaded structure which locally breaks the interaction between the electron beam and the slow wave structure supported by the periodic configuration.

D. Magnetic field-gradient effects

An important difference between the QOG configuration and the CCG is found in the magnetic field gradients experienced by the electron beam traveling from the cathode to the interaction region. For the latter configuration, these gradients are significantly larger than for the QOG. A relevant quantity for comparing the magnetic field gradient of different gyrotron configurations is the magnetic field variation over a cyclotron wavelength $\lambda_c = \dfrac{2\pi c\gamma}{\Omega_{cemax}}$, where Ω_{cemax} is the maximum cyclotron frequency along the magnetic field profile. Figure 19 shows the dependence of $\lambda_c \dfrac{dB}{dz}$ for two QOG and for two cylindrical cavity gyrotrons where the position $z = 0$ represents the center of the

gyrotron cavity. For the 100 GHz QOG one observes an extremely long section in the beam tunnel region where the gradient is small, the double hump magnetic field profile of the 90 GHz QOG makes that a zero gradient section is found inside the beam tunnel where the pitch angle is simultaneously maximum. Conversely, for the cylindrical cavity configurations, the gradients are always larger and the flat portion of the magnetic field profile is found at the entrance of the interaction region. As it has been discussed earlier, the Bernstein and Langmuir instabilities are relatively insensitive to magnetic field gradient whereas the ECM instability shows a very strong dependence and the excitation of parasitic oscillations in the beam tunnel is favored in a QOG.

V. CONCLUSIONS

An experimental study dedicated to the observation of parasitic modes in a gyrotron beam tunnel has been presented. The observed radiation is due to the Electron Cyclotron Maser instability which excites eigenmodes of the beam tunnel (parasitic modes) at beam currents levels much lower than the minimum starting current of a TEM mode supported by the Fabry-Pérot resonator. Even at low power levels, the parasitic modes can induce a significant energy spread in the electron beam which significantly lowers the gyrotron interaction efficiency. It is shown that the excitation of parasitic modes is strongly dependent on the geometry of the beam tunnel, the geometrical structure of the dielectric loading and the magnetic field gradient in the beam tunnel. Experimental evidence shows that an aperiodic stack of conducting and dielectric rings suppresses the parasitic modes in the beam tunnel, despite the unfavorable low-gradient magnetic field configuration.

At high power level, the required beam current and cross section makes that the electron beams presently designed for QOG have an electron density higher than for an equivalent cylindrical cavity configuration. For the presently designed electron beams, the electrostatic Bernstein instability can grow to a level at which the induced energy

spread can significantly reduce the interaction efficiency. This type of instability is only dependant on the beam density and in order to decrease it, larger radius or thicker beams are required. Theoretical calculations are presently underway which will eventually allow to a beam optimization with lower beam densities.

A discussion on the excitation of electrostatic Langmuir instabilities in a periodic beam tunnel is made. In order to prevent the excitation of such waves, the aperiodic loaded beam tunnel described above for the suppression of the electromagnetic instability would simultaneously suppress the Langmuir instability.

ACKNOWLEDGMENTS

The authors would like to thank Dr.J. Vomvoridis, Dr.I. Tigelis, Dr. K. Appert and G. Jost for helpful discussions. This work was partially supported by the Office Fédéral de l'Energie under grants OFEN-EF-FUS(91)-01 and OFEN-Gyrotron 581 233, and by the Fonds National Suisse pour la Recherche Scientifique.

REFERENCES

[1] Y.Y. Lau, J. Appl. Phys. **61**, 36, (1987).

[2] V.K. Lygin, Int. J. Infrared Millimeter Waves **16**, 363, (1995).

[3] C. Liu, T.M. Antonsen, and B. Levush, IEEE Trans. on Plasma Science **24**, 982, 1996.

[4] B. Piosczyk, in Proceedings of 18th International Conference on Infrared and Millimeter Waves, Colchester, 1993, edited by J.R. Birch and T.J. Parker, (SPIE The International Society of Optical Engineering, Bellingham, Washington, 1993), Vol. 2104, p. 450.

[5] W.C. Guss, T.L. Grimm, K.E. Kreischer, J.T. Polevoy and R.J. Temkin, J. Appl. Phys. **69**(7), 3789 (1991).

[6] G. Soumagne, S. Alberti, J.P. Hogge, M. Pedrozzi, M.R. Siegrist, M.Q. Tran, M.T. Tran, Phys. Plasmas **3**, 3501, 1996.

[7] S. Alberti, M.Q. Tran, J.P. Hogge, T.M. Tran, A. Bondeson, P. Muggli, A. Perrenoud, B. Jödicke, and H.G. Mathews, Phys. Fluids **B2**, 1654 (1990).

[8] J.P. Hogge, T.M. Tran, P.J. Paris, M.Q. Tran, Phys. Plasmas **3**, 3492, 1996.

[9] M. Pedrozzi, S. Alberti and M.Q. Tran, in Proceedings of 20th International Conference on Infrared and Millimeter Waves, Orlando, 1995, edited by R.J. Temkin, p. 134.

[10] I.I. Antakov, I.G. Gachev, E.V. Zasypkin., IEEE Trans. on Plasma Science **22**, 878, 1994.

[11] T.M. Tran, G. Jost, K. Appert, S. Alberti, M. Pedrozzi, Phys. Plasmas **4**, 3043 (1997).

[12] A. Bondeson, T.M. Antonsen, Int. J. Electronics **61**, 855 (1986).

[13] V.L. Bratman, A.V. Savilov, Phys. Plasmas **2**, 557 (1995).

[14] A.V. Savilov, Phys. Plasmas **4**, 2276 (1997).

[15] J.L. Vomvoridis, I.G. Tigelis, in Proceedings of 21st International Conference on Infrared and Millimeter Waves, Berlin, 1996, edited by M. von Ortenberg and H.H Mueller, (ISBN 3-00-000800-4).

[16] I.G. Tigelis, M. Pedrozzi, P.G. Cottis, J.L. Vomvoridis, IEEE Trans. on MTT **45**, 236, 1997.

[17] B.G. Danly, R.J. Temkin, Phys. Fluids **29**, 561 (1986).

[18] A.W. Fliflet, T.A. Hargreaves, R.P. Fisher, W.M. Manheimer, P. Sprangle, Journal of Fusion Energy **9**, 31 (1990).

[19] D.R Whaley, T.P. Goodman, A. Pochelon, R. Behn, A. Cardinali, B.P. Duval, B. Joye, M.Q. Tran, Nuclear Fusion **32**, 757 (1992).

[20] S. Alberti, O. Braz, P. Garin, E. Giguet, M. Pain, P.H. Thouvenin, M. Thumm, C. Tran, M.Q. Tran, in Proceedings of 21th International Conference on Infrared and Millimeter Waves, Berlin, 1996, edited by M. von Ortenberg and H.U. Mueller, (ISBN 3-00-000800-4) p. AF1.

[21] S. Alberti, M.Q. Tran, T.M. Tran, Phys. Fluids B **3**, 519 (1991).

[22] P.E. Latham, *private communication* .

[23] K.E. Kreischer, R.J. Temkin, Infrared and Millimeter waves Vol.7, Edited by K.J. Button, Academic Press, Inc., 377 (1983)

[24] G.S. Nusinovitch, Int. J. Electronics **64**, 127 (1988).

[25] P.E. Latham, S.M. Miller, C.D. Striffler, Phys. Rev. A **45**, 1197 (1992).

[26] T. Goodman, M. Henderson, A. Pochelon, S. Alberti, M.Q. Tran, in "Strong Microwaves in Plasmas", Proceedings of the International Workshop, Institute of Applied Physics, Nizhny Novgorod University Press, 1997, edited by A.G. Litvak, (ISBN 5-201-09305-1), p. 35.

[27] G. Jost, T.M. Tran, K. Appert, S. Wütrich, Comput. Phys. Commun. **100**, 47 (1997)

TABLES

instability	growth rate	frequency
ECM	$\omega_i \propto \omega_{pe}^{\frac{2}{3}}(\frac{\beta_\perp^2}{\gamma_0})^{\frac{1}{3}} \propto (I_b\frac{\beta_\perp^2}{\gamma_0})^{\frac{1}{3}}$	$\frac{\omega_r}{2\pi} \approx s\frac{\Omega_{ce}}{\gamma 2\pi}$
Bernstein	$\omega_i \propto \omega_{pe}\frac{\beta_\perp}{\sqrt{\gamma_0}} \propto \sqrt{I_b}\frac{\beta_\perp}{\sqrt{\gamma_0}}$	$\frac{\omega_r}{2\pi} \approx s\frac{\Omega_{ce}}{\gamma 2\pi}$
Langmuir	$\omega_i \propto (\omega_{pe})^{\frac{2}{3}}\beta_z v_g \propto (I_b)^{\frac{1}{3}}\beta_z v_g$	$\omega_r \approx k_z c\beta_z$

TABLE I. Temporal linear growth rates and frequencies of the three instabilities, with $\omega_{pe} = n_b e^2/m_0\epsilon_0$ the non-relativistic plasma frequency, where n_b is the electron beam density, e the electron charge, m_0 the electron mass and ϵ_0 the vacuum permittivity. The quantities I_b, s, v_g are the beam current, the cyclotron harmonic number and wave group velocity, respectively.

Gyrotron	η_{theory}	$\eta_{exp.}$
QOG 100 GHz [7]	22%	12%
QOG 90 GHz [8]	23%	16%
QOG 120 GHz [18]	23%	12%
CCG 39 GHz [19]	44%	42%
CCG 118 GHz [20]	34%	34%

TABLE II. Gyrotron efficiency comparison between quasi-optical gyrotrons (QOG) and cylindrical cavity gyrotrons (CCG).

material	ε_r	$\tan\delta = \frac{\varepsilon_i}{\varepsilon_r}$
MgO (95%)-SiC(5%)	12.54	0.053
AlN (60%)-SiC(40%)	26	0.29
Robax (Trademark)	5.72	0.058

TABLE III. Absorbers dielectric properties @ 100GHz.

FIGURES

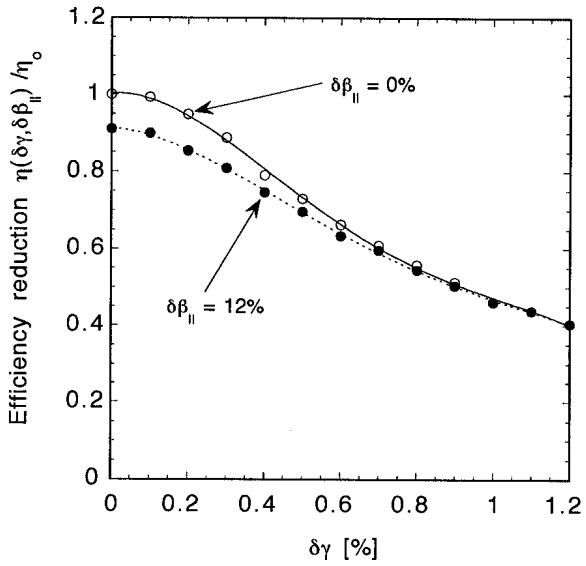

FIG. 1. Calculated efficiency reduction $\eta(\delta\gamma, \beta_{||})/\eta_0$ $[\eta_0 = \eta(\delta\gamma = 0, \delta\beta_{||} = 0)]$ as a function of the energy spread $\delta\gamma$ and for two different parallel velocity spreads $\delta\beta_{||} = 0\%, 12\%$. A Gaussian rf profile is considered with a normalized interaction length $\mu = 18$ [17] ($\langle\alpha\rangle = 1.5$, $\langle\gamma\rangle = 1.137$) and a pencil beam with a beam current of $I_b = 10$A. The distribution functions for the energy and parallel velocity are gaussian.

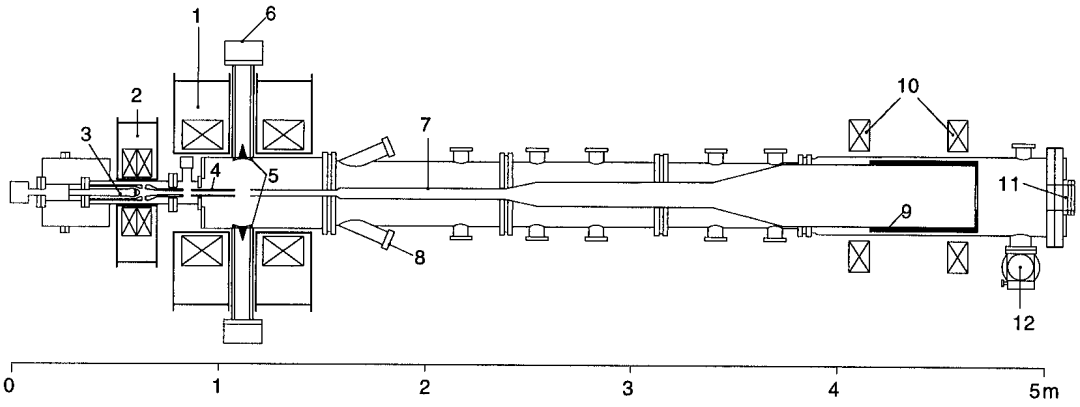

FIG. 2. Experimental set up. 1 Helmholtz coils. 2. Gun coils. 3. Electron gun (MIG). 4. Beam tunnel before resonator. 5. Fabry-Pérot resonator. 6. Output window. 7. Beam tunnel after resonator. 8. Lateral window. 9. Collector. 10. Collector coils. 11 Collector window. 12. Pump.

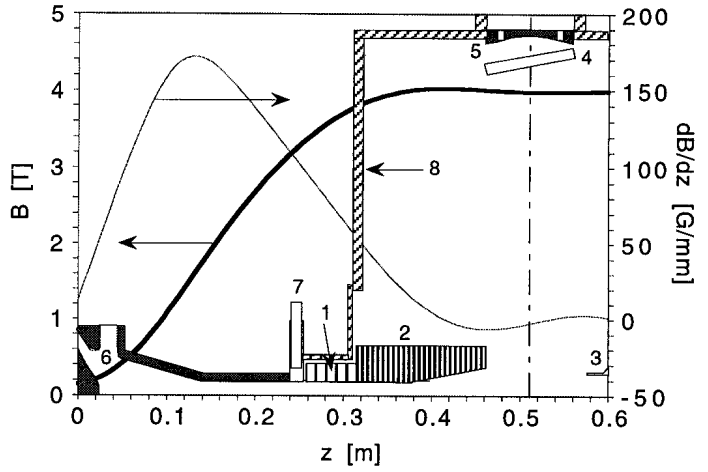

FIG. 3. Magnetic field and magnetic field gradient profiles with details of experimental set up. 1. Beam tunnel (section 1), 2. Beam tunnel (section 2), 3. Beam tunnel (section 3), 4. Macor plate, 5. Fabry-Pérot resonator, 6. Magnetron Injection Gun, 7. Gun valve, 8. Vacuum vessel.

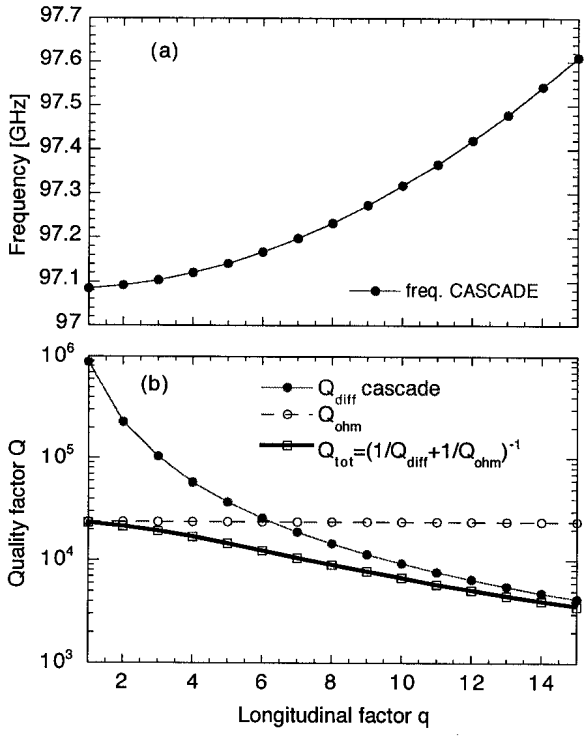

FIG. 4. Calculated resonant frequencies a) and diffractive, ohmic and total quality factors b) for the $TE_{0,3}$ mode versus longitudinal index q.

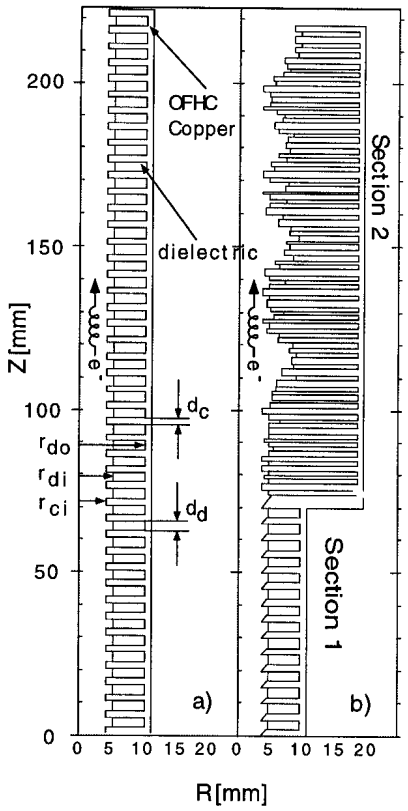

FIG. 5. Dielectrically loaded beam tunnels. a) is a periodic structure and b) is aperiodic. The portion of beam tunnel labeled "section 2" corresponds to "section 2" in Fig. 3.

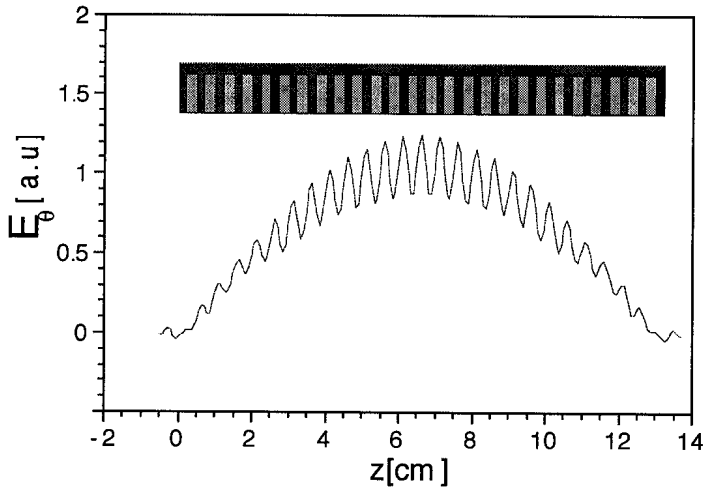

FIG. 6. Calculated electric field profile (E_θ) at the resonance in periodic loaded beam tunnel (MgO-SiC). Copper rings: r_{ci} = 5mm, d_c = 2mm. Dielectric rings: r_{di} = 5mm, r_{do} = 11mm, d_d = 3mm. The resonant frequency is 97.9 GHz and the radial profile for $r < r_{ci}$ is like the TE_{03} profile of a smooth beam duct.

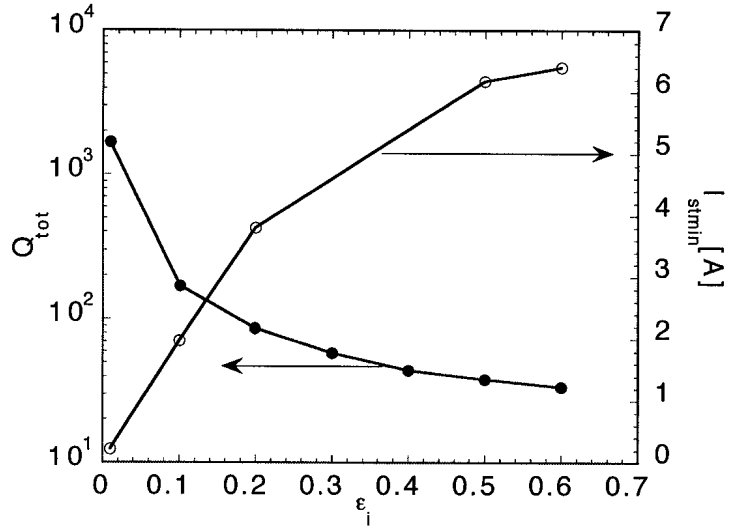

FIG. 7. Computed total quality factor and minimum starting current versus ε_i ($\varepsilon_r = 12.54$, MgO-SiC) for the periodic beam tunnel (TE_{03}^{eq}, $f = 97.9$GHz see Fig. 6).

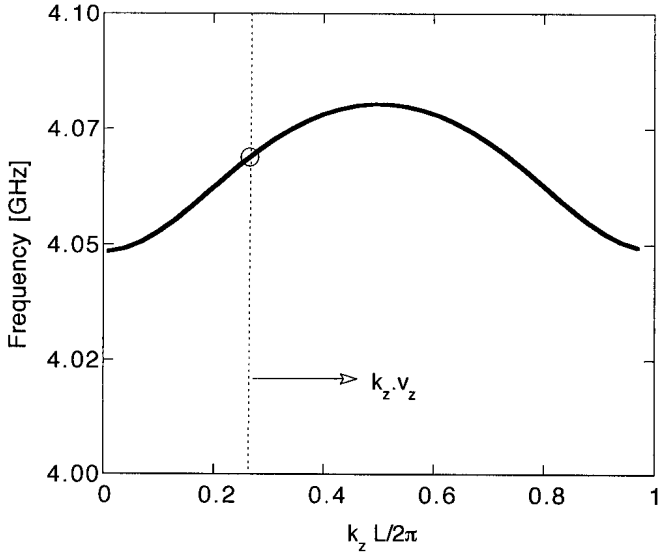

FIG. 8. Slow-wave dispersion relation in the periodic beam tunnel (thick line). The transverse profile of this mode under a copper disk is TM_{01} like and the beam parameters corresponding to the beam line (dotted line) are: $V_b = 70$kV and $\alpha = 1.2$. The open circle shows the intersection between the beam line and the dispersion relation giving the frequency at which the instability could be excited.

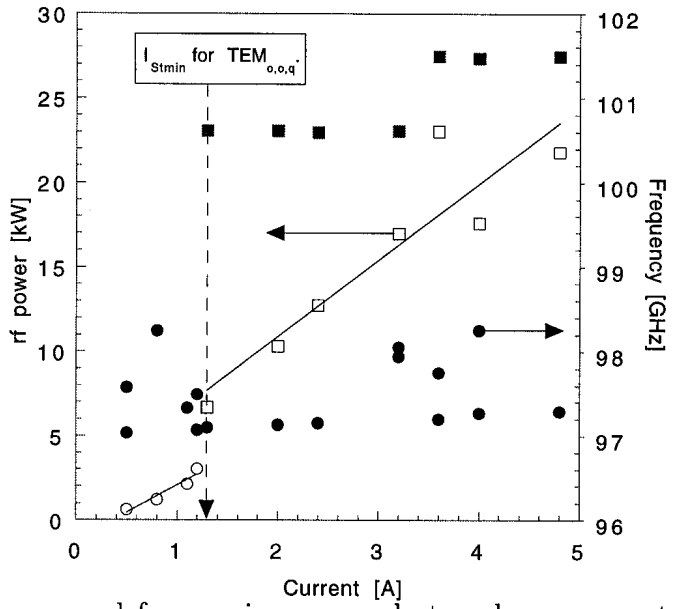

FIG. 9. QOG power and frequencies versus electron beam current with the Fabry-Pérot resonator in place and a periodic beam tunnel. Parasitic oscillation frequencies are represented by filled circles whereas empty circles represent an estimation of the parasitic rf-power. Frequencies associated to TEM_{00q} modes supported by the Fabry-Pérot resonator are represented by filled squares. Empty squares describe the total rf-power (parasitic and Fabry-Pérot mode) measured at the output window.

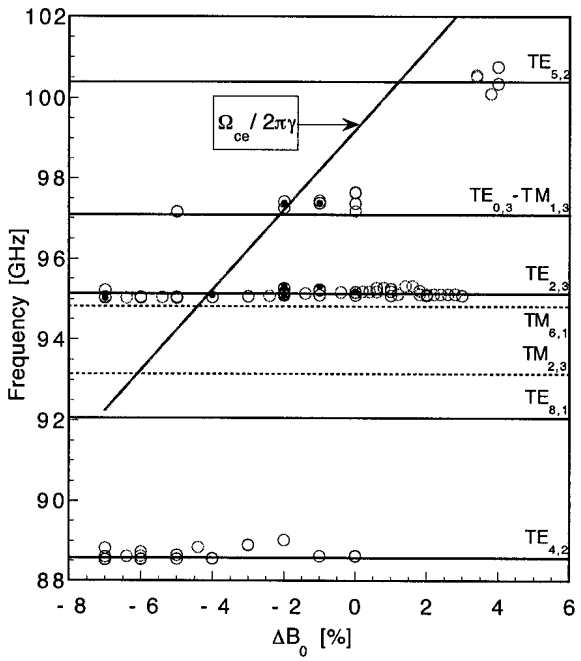

FIG. 10. Parasitic frequencies excited in the smooth beam tunnel versus magnetic field variation. The electron beam parameters are: $V_b = 66\text{kV}$, $\langle\alpha\rangle = 0.92$, $I_b = 100 - 700\text{mA}$, $B_0 = 4\text{T}$ @ $\Delta B_0 = 0$.

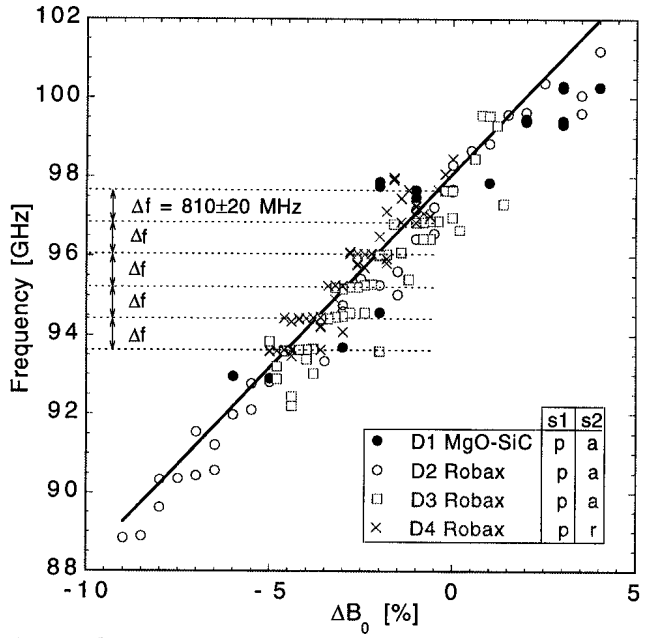

FIG. 11. Parasitic mode excitation versus magnetic field variation with aperiodic beam tunnel for different types of configuration and dielectric (V_b = 73kV, B_0 = 4T @ $\Delta B_0 = 0$, $\langle\alpha\rangle = 1 - 1.5$, $I_b = 250 - 800$mA). The columns "s1" and "s2" in the table give the type of structure of section 1 and 2 (c.f. Fig. 5), respectively. For the configurations D3 and D4, the copper ring was wedge shaped as indicated in Fig. 5. The abbreviations ,"p", "a" and "r" stand for periodic, aperiodic and removed, respectvely.

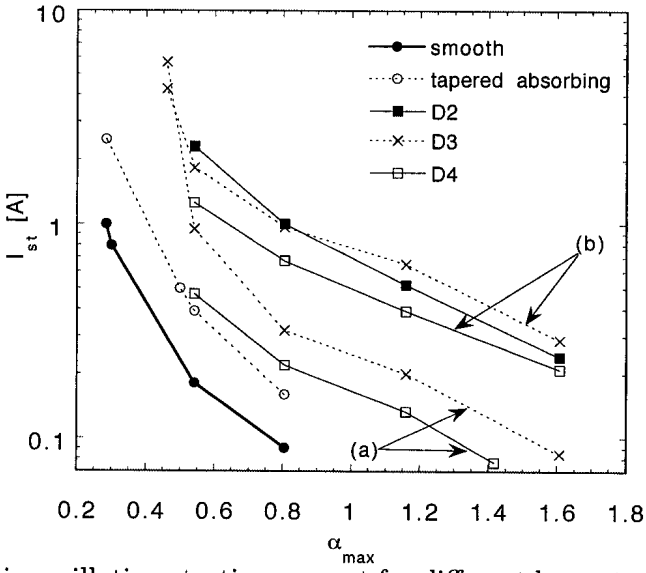

FIG. 12. Parasitic oscillation starting current for different beam tunnel configurations. The configurations labeled D2, D3 and D4 are listed in Fig. 11 (V_b = 66kV, B_0 = 4T).

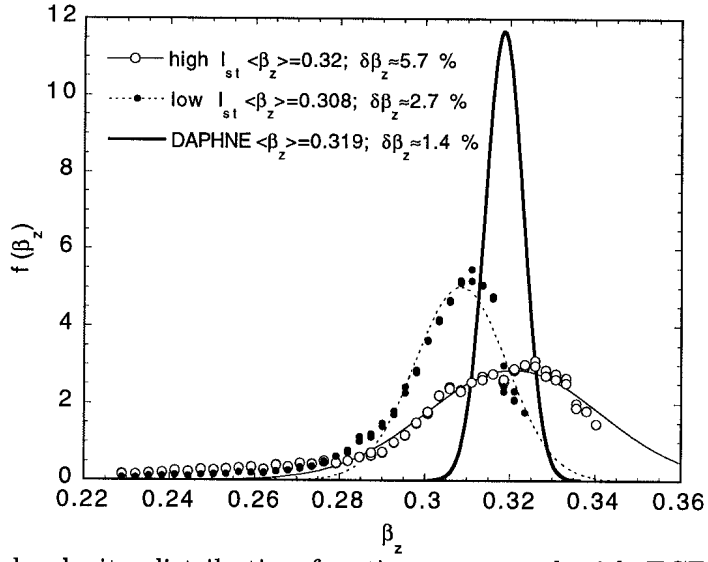

FIG. 13. Parallel velocity distribution functions measured with ECE diagnostic for two different MIG regimes (V_b = 62kV, $\langle\alpha\rangle$ = 1, I_b = 500mA). The thick continuous line corresponds to the distribution (assumed to be gaussian) given by the trajectory code DAPHNE, the dotted line and the thin continous line are least-square fit of a gaussian distribution on the experiemental datas.

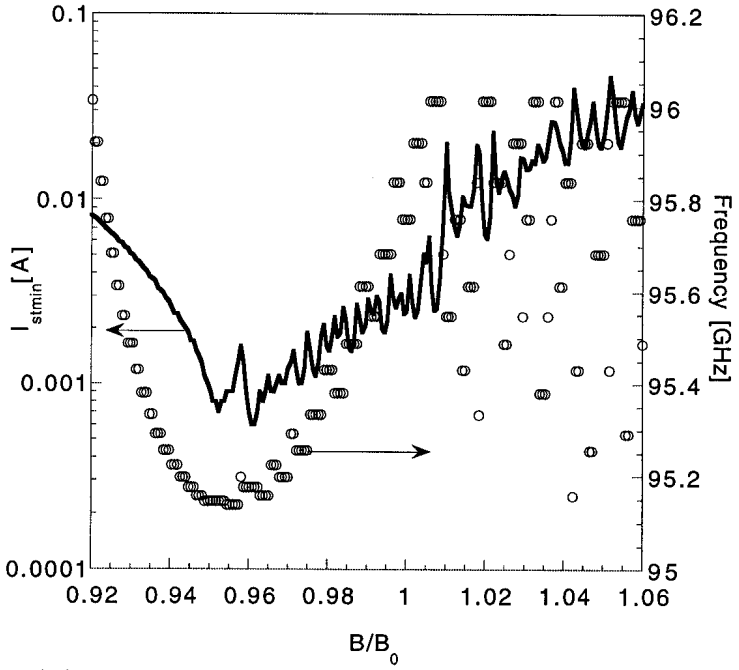

FIG. 14. $TE_{2,3,q}$ minimum starting current for $q = 1 - 20$ versus magnetic field variation B/B_0 (V_b = 67kV, B_0 = 4T, $\langle\alpha\rangle$ = 1, r_b = 2.4mm, r_w = 5mm).

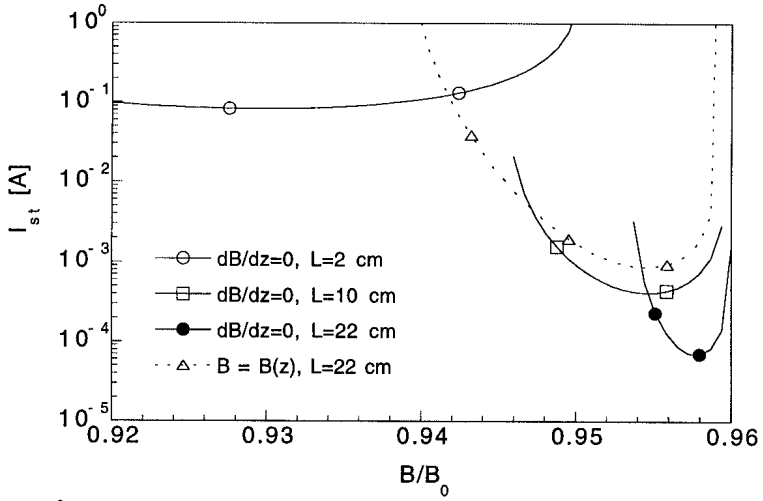

FIG. 15. Influence of interaction length on the starting current for a uniform magnetic field and for the actual profile. Resonant mode: $TE_{2,3,1}$ and the beam parameters are, $B_0 = 4T$, $r_w = 5mm$, $r_b = 2.4mm$, $V_b = 66.5kV$, $\alpha = 1$.

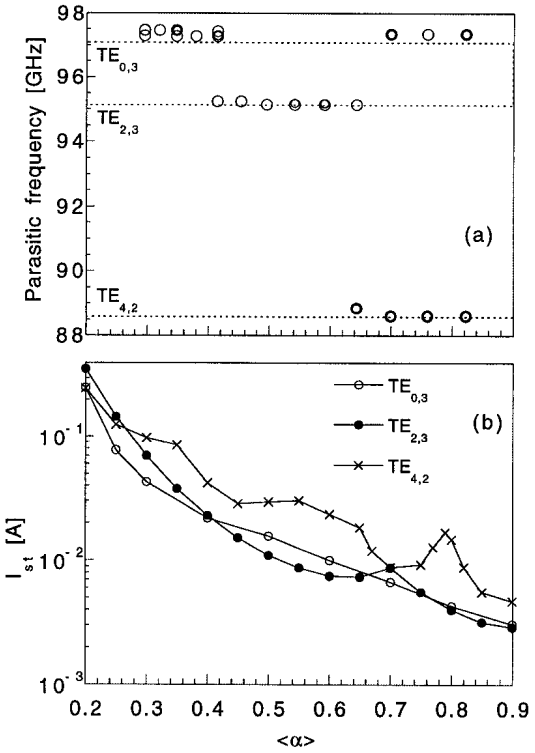

FIG. 16. Parasitic mode excitation versus α for the smooth beam tunnel configuration. a) Measured frequencies ($V_b = 66kV$, $B_0 = 4T$, $I_b \simeq 1A$), b) Calculated minimum starting current.

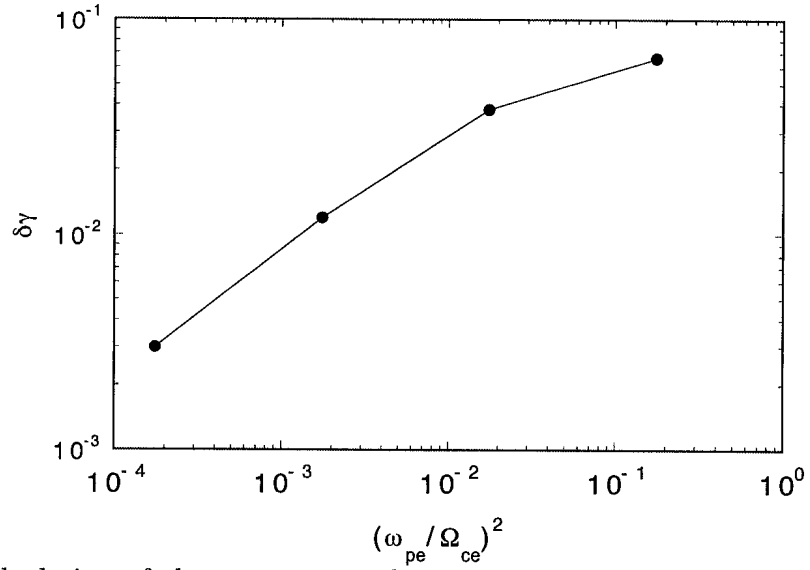

FIG. 17. 2D calculation of the energy spread induced by the Bernstein instability [11]. Constant magnetic field.

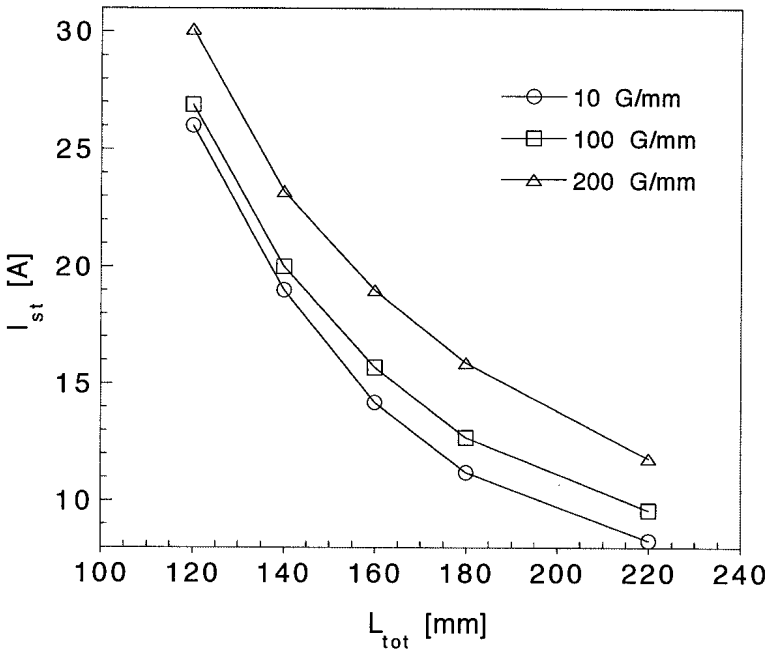

FIG. 18. Langmuir instability starting current for the periodic beam tunnel for a linearly tapered magnetic field. The dispersion relation for the periodic structure and the beam properties are described in Fig.8.

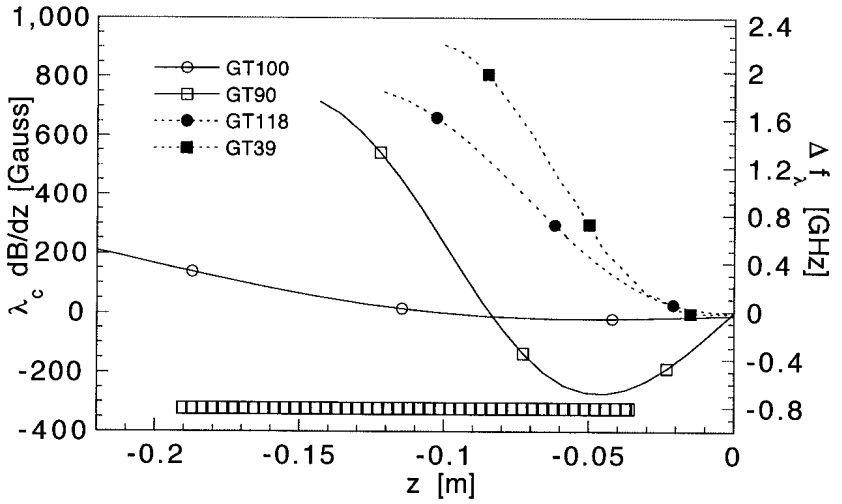

FIG. 19. Magnetic field and cyclotron frequency variation over the caracteristic length λ_c for two QOG configurations (GT100 and GT90) and for two CCG (GT118 and GT39).